An Improved Ambiguity Echo Separation Strategy for Multichannel SAR Based on Independent Component Analysis

Yuhao Wen , Zhimin Zhang, Xiangrui Meng , Zongsen Lv , Zhen Chen , *Member, IEEE*, Yifei Liu , Huaitao Fan , and Lei Zhang

Abstract—High-resolution, wide-range imaging is crucial for contemporary and future remote sensing surveys. Multichannel synthetic aperture radar (SAR) is an effective tool to fulfill this requirement. Among various multichannel technologies, null steering digital beamforming is commonly used for ambiguity suppression, SAR echo separation, and interference and clutter suppression. However, existing null steering beamforming algorithms lack robustness and are sensitive to channel errors. This article proposes an improved SAR echo separation scheme based on complex independent component analysis (ICA) to address the channel error issue. Initially, the problem caused by channel error leading to the failure of the linear constraint minimum variance (LCMV) beamformer is analyzed. Then, non-Gaussian and non-circular measurements of SAR echoes from different scatterers are conducted, concluding that multichannel SAR echoes satisfy the conditions for ICA application. For an elevated multichannel wide-swath SAR, an ambiguity signal separation scheme based on ICA is proposed. Block processing or pure-decimal-constraint LCMV (PDC-LCMV) beamforming is first employed to compensate for the spatial dependence of the mixing matrix. A complex entropy-bound maximum algorithm, based on source signal independence, is then used for further signal separation. Our proposed scheme effectively addresses the channel error issue in traditional null steering beamforming schemes and efficiently separates ambiguity echoes. It leverages the statistical characteristics of the signal itself and expands the processing dimension. Capable of handling multiple errors, it is suitable for systems with limited degrees of freedom and does not require additional hardware resources. Simulation experiments verify the effectiveness of this scheme.

Index Terms—Channel errors, independent component analysis (ICA), null steering beamforming, synthetic aperture radar (SAR).

Yuhao Wen, Xiangrui Meng, Zongsen Lv, and Yifei Liu are with the Department of Space Microwave Remote Sensing System, Aerospace Information Research Institute, Chinese Academy of Sciences, Beijing 100190, China, and also with the School of Electronic, Electrical and Communication Engineering, University of Chinese Academy of Sciences, Beijing 100039, China (e-mail: wenyuhao19@mails.ucas.ac.cn).

Zhimin Zhang, Zhen Chen, Huaitao Fan, and Lei Zhang are with the Department of Space Microwave Remote Sensing System, Aerospace Information Research Institute, Chinese Academy of Sciences, Beijing 100190, China (e-mail: chenzhen@aircas.ac.cn).

I. INTRODUCTION

IN THE field of remote sensing, synthetic aperture radar (SAR) has the capability of perceiving multidimensional information about the Earth, and it has the advantages of all-weather, all-day, and strong penetrative abilities compared to optical radars. Currently, SAR has been widely used in land exploration, disaster monitoring, military reconnaissance, and other fields [1], [2]. High-resolution wide-swath imaging is an important development direction of SAR currently and in the future. The significance of high-resolution lies in improving the accuracy of SAR observation, detection, identification, and classification of targets; and the significance of wide swath lies in shortening revisit cycles and increasing the efficiency of remote sensing observations. As an imaging radar, the observation swath width is a key indicator of its measurement efficiency. Especially for applications such as ocean monitoring and map mapping, there is a high demand for the wide-swath imaging capability of SAR. However, due to the pulse transceiver system of traditional SAR, there is a tradeoff between the imaging resolution and the swath, which can be described by the minimum antenna area constraint [3], [4]. Therefore, when considering the SAR system design, the two performance indicators of high resolution and wide swath are supposed to be balanced. With hardware upgrades, multibeam and multichannel SAR systems are gradually being used to further enhance SAR observation flexibility [5]. The single-phase center azimuth multibeam technology utilizes multiple azimuth-receiving beams to reduce the system's PRF requirements [6]. The displaced phase center antenna (DPCA) technology in azimuth replaces time sampling with spatial sampling to overcome the swath width restriction while satisfying the Doppler bandwidth sampling requirements [7]. The elevated multibeam technology separates range ambiguity echoes and enables wide-swath observation through spatial beamforming techniques [6], [8], [9]. Subsequently, a 2-D multichannel quad-element SAR and a high-resolution wide-swath system are proposed [10], [11]. In these two systems, the azimuth channels are used for the DPCA technique while the elevated channels are employed to enhance the image signal-to-noise ratio [10] or suppress range ambiguity [11]. With the complexity increasing, the multidimensional waveform encoding SAR, combining the multichannel structure and the signal encoding technique, enhances system observation flexibility [12], [13], [14], [15],

[16]. In addition to the multiple-input single-output systems mentioned before, multi-input multioutput (MIMO) SAR and multistatic SAR systems can also provide additional degrees of freedom for high-resolution wide-swath imaging in extra dimensions [17], [18], [19].

Spatial beamforming technology is often used for ambiguity suppression, signal separation, clutter suppression, and jamming suppression in multichannel SAR systems, which is a key technology for high-resolution wide-swath imaging. However, this technology is limited by channel errors in practical multichannel SAR applications [20]. Severe errors may lead to performance degradation or even system failure. Common methods for compensating multichannel SAR channel errors include time-domain correlation [21], orthogonal subspace method [22], and signal subspace comparison [23]. However, these methods have their limitations. They may fail or leave residual errors in practical applications.

In spatial beamforming technologies, the optimal beamformers such as linear constraint minimum variance (LCMV) and minimum variance distortionless response (MVDR) are commonly used for their good suppression effect on the ambiguity, clutter, and jamming [24], [25]. The LCMV and MVDR beamformers can optimize the weighted vectors through model design to enhance the desired signals with the main lobe and suppress the unexpected signals with the beam pattern nulls. Thus, they also called the null-steering digital beamforming algorithms. Few literature studies have investigated the high sensitivity of these optimal beamformers to channel errors when applied to multichannel SARs. Hence, it is necessary to investigate methods for further improving the robustness of spatial filtering in the presence of residual errors. Additionally, for multichannel SARs, the channel arrangement needs to be reasonably designed according to the desired beamforming requirements in subsequent stages.

Similar to spatial beamforming technology, blind source separation (BSS) is an efficient signal separation method in the field of array signal processing [26]. As a representative BSS algorithm, independent component analysis (ICA) is commonly used to separate signals from mixed signals based on their statistical independence [27]. It has been widely applied in areas, such as speech signal processing and biological signal processing [28], [29]. In the field of remote sensing, ICA is typically used for hyperspectral remote sensing image analysis, image classification, and more [30]. Chen et al. [31] attempted to use ICA for interference signal separation in SAR systems. Chang et al. [32] used the second-order blind identification algorithm for SAR range ambiguity suppression. Generally, the application of ICA in the SAR echo signal domain is relatively limited.

Despite the existing channel calibration algorithms being able to achieve high accuracy, there are still residual errors in certain situations. This problem can cause distortions in the beamforming direction, potentially affecting the performance of multichannel wide-swath SAR systems based on spatial filtering. In response to this issue, this article proposes a multiswath echo separation optimization method based on SAR echo statistical characteristics in a multiswath MIMO-SAR imaging system.

This method can alleviate channel errors and effectively improve the high-resolution wide-swath remote sensing performance of SAR.

The main contributions of this article are as follows.
1) Based on Sentinel-1 A data, the statistical characteristics of SAR echo data from different terrains have been analyzed, including non-Gaussianity and noncircularity. We propose to measure the statistical differences of SAR echo signals using the complex signal skewness and the noncircularity coefficient.
2) A novel framework for optimizing SAR signal separation is proposed in this study. The framework is based on the theory of ICA, leveraging the statistical characteristic differences, specifically non-Gaussianity and noncircularity, between the desired signal and the ambiguous signal to achieve improved separation performance. This framework effectively addresses the issue of separation failure resulting from residual channel errors.
3) The effectiveness of the proposed method was comprehensively validated through simulated experiments. The normalized ambiguity power was employed as a parameter to measure the signal separation performance.

The rest of the article is organized as follows. Section II describes the channel error issue in multichannel wide-swath SAR systems and briefly introduces the theory of linear BSS. Section III provides a detailed introduction to an optimized method for echo separation based on the statistical characteristics of SAR echoes. Section IV presents the simulation results of point-target and distributed scatterers. Section V validates the proposed method using real data. Finally, Section VI concludes this article.

II. PROBLEM STATEMENT

A. Interchannel Errors in Multichannel Wide-Swath SAR

Traditional SAR systems encounter a fundamental tradeoff between high azimuth resolution and a wide range swath. To resolve this challenge, early studies introduced various operational modes, including spotlight, sliding spotlight, scanning SAR (ScanSAR), and terrain observation with progressive scans SAR (TOPSAR), which enable the system to strike a balance between resolution and swath width based on precise application demands. The underlying cause of this tradeoff dilemma can be traced back to the pulse transmission mode employed by SAR systems. In the case of single-channel strip mode SAR systems, the maximum range direction imaging swath width can be determined as

$$R_{\mathrm{u}} = \frac{\mathrm{c}}{2\mathrm{PRF}} \tag{1}$$

where c is the light velocity, and PRF is the pulse repetition frequency. Once the observed swath exceeds R_{u}, echo signals from different distances will be sampled concurrently and overlap in the time domain, resulting in range ambiguity in SAR images.

The multichannel SAR can further enhance system degrees of freedom in order to break the mutual constraint between high resolution and wide swath. Typically, azimuth multichannel

systems increase spatial sampling to cover a wider Doppler bandwidth, thus improving the upper limit of azimuth resolution while maintaining the swath width constant. In an elevated multichannel system, range ambiguity can be addressed using spatial filtering, which is essentially null-steering beamforming. Various systems, including elevated single-phase center multibeam systems, spatial time waveform encoding SAR [8], wide-swath MIMO-SAR, have utilized this technique. As the supervisor suppression capacity to other null-steering algorithms, the LCMV beamformer is widely applied for range ambiguity suppression, which can be described as

$$\begin{cases} \min_{\boldsymbol{w}} & \boldsymbol{w}^{\mathrm{H}} \boldsymbol{R}_{\mathrm{n}} \boldsymbol{w} \\ \text{s.t.} & \boldsymbol{w}^{\mathrm{H}} \boldsymbol{C} = \boldsymbol{e}^{\mathrm{H}} \end{cases} \quad (2)$$

where $\boldsymbol{\omega}$ is the weighting vector, $\boldsymbol{R}_{\mathrm{n}}$ is the correlation matrix of the thermal receiver noise, $\boldsymbol{C}$ is the constraint matrix consisting of manifold vectors of the distortionless response constraint and null constraints, and $\boldsymbol{e}$ is the constraint vector. $(\cdot)^{\mathrm{H}}$ is the conjugate transpose operator. Assuming the white noise model with expectation as 0, and covariance as σ_n^2, the previous optimization model can be solved as

$$\boldsymbol{w} = \boldsymbol{e}^{\mathrm{H}} \left[\boldsymbol{C}^{\mathrm{H}} \boldsymbol{C} \right]^{-1} \boldsymbol{C}^{\mathrm{H}}. \quad (3)$$

The robustness of beamformers refers to the extent of performance degradation in the presence of errors. According to (2), the robustness of LCMV is mainly affected by the accuracy of the array response vector and the estimation of the covariance matrix. In practice, channel errors, orbit bias, attitude offset, and bias of direction of arrival may all become the influence factor. In the application discussed in this article, the spatial information of the desired signal and ambiguous signal is known a priori, so we only consider the influence of channel errors on the beamformer performance. Despite there are some calibration errors for channel errors, residual terms still exist in practice. Typically, channel errors in multichannel systems are divided into amplitude error, phase error, range synchronous time error, and unexpected channel position variation. These errors stem from hardware discrepancies between different channels, including amplitude errors caused by amplifier variations constant phase errors caused by hardware differences, and time delay errors caused by cable differences or array deformation. Specifically, channel errors lead to mismatches in the array response vector, resulting in a distorted main lobe, deviated null-steering, and degraded nulling capacity. Fig. 1(a) gives the LCMV beam pattern of a 10-element linear array with and without channel errors. With only around $5°$ constant phase errors in every channel, the nulling capacity of the LCMV beamformer degrades, and the interferences at $30°$ and $50°$ are not properly suppressed. Fig. 1(b) gives the trend of output signal-to-interference-ratio (SINR) loss of the LCMV beamformer changing with error variance. One can see that the SINR loss grows up when the variance increases.

B. Linear Instantaneous Signal Mixture Model

Blind signal processing constitutes a significant branch within the realm of array signal processing. It entails a technique that
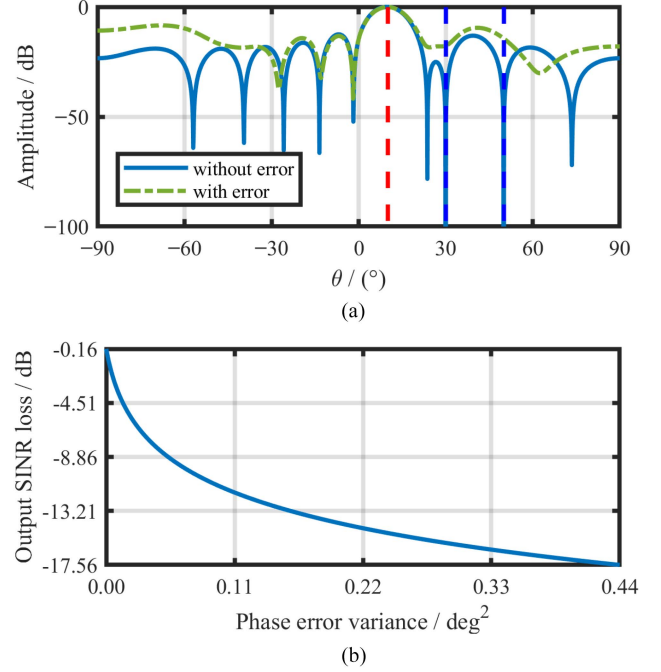

Fig. 1. LCMV with array errors. (frequency: 9.6 GHz, array length: 0.15 m, array element number: 10, signal power: 20 dB, interference power: both 35 dB, noise power: 0 dB). (a) LCMV beam patterns with and without channel errors. (b) LCMVs SINR loss changes with phase error variance.

estimates the source signals and system transmission matrix by analyzing the system output signals. This technique finds crucial applications in various fields, such as wireless communication, image processing, biomedical signal processing, and speech signal processing. One of the key challenges in blind signal processing is BSS technology, which aims to accurately estimate the source signals based on the observed mixed signals. Depending on the characteristics of source signal mixing, BSS problems can be broadly categorized as linear or nonlinear. As the term suggests, linear BSS problems involve obtaining output signals through the linear mixing of the source signals. Specifically, this category of problems can be further divided into linear instantaneous mixing and linear convolution mixing. The following section describes the mathematical model for the linear instantaneous mixture problem:

$$\begin{cases} \boldsymbol{y}(k) = \boldsymbol{A}\boldsymbol{s}(k) \\ \boldsymbol{y}(k) \in \mathbb{C}^{M \times 1} \\ \boldsymbol{A} \in \mathbb{C}^{M \times N} \\ \boldsymbol{s}(k) \in \mathbb{C}^{N \times 1} \end{cases} \quad (4)$$

where $\boldsymbol{y}(k)$ is the vector of M observed signals, $\boldsymbol{A}$ is the mixing matrix, $\boldsymbol{s}(k)$ is the vector of N source signals, and k is the discrete time. When $M > N$, the model belongs to the overdetermined BSS model. When $M = N$, it is the determined model. And when $M < N$, it is the underdetermined model. The goal is to find a separation matrix $\boldsymbol{D}$ and obtain an estimation $\widehat{\boldsymbol{s}}(k)$ of the source signals, given only $\boldsymbol{y}(k)$.

In BSS algorithms, high-order parameters, such as non-Gaussianity, noncircularity, nonwhiteness, and nonstationarity,

are employed to describe the statistical characteristics. These algorithms rely on three conditions for their application. First, the source signals must exhibit statistical independence. Second, only one of the source signals should potentially follow a Gaussian distribution. Finally, the dimension of the observation should be equal to or exceed the dimension of the source signals.

Analyzing the aforementioned BSS model bears a similar form to the problem of echo separation in multichannel SAR systems. This similarity indicates the potential application of BSS algorithms to SAR echo signals. Moreover, SAR echo signals typically exhibit statistical independence among signals from different objects. Additionally, multichannel SAR systems offer sufficient observation dimensions. One can say the SAR echo satisfies the first and the third conditions for the BSS model. Applying BSS algorithms requires further analysis of the statistical characteristics inherent in SAR echo signals.

III. STATISTICAL ANALYSIS OF SAR ECHO SIGNALS

Due to the complex mechanism of SAR image formation, SAR data cannot be completely modeled deterministically, requiring consideration of the randomness in echo signals. The echo signal is influenced by geometric and electromagnetic characteristics of measured scatterers, including relative permittivity, conductivity, macroscopic roughness, and microscopic roughness. While electromagnetic characteristics can be inferred from the object type, geometric features, such as scene roughness, necessitate a statistical framework for description. Consequently, SAR echo data can be described as a stochastic process.

As a kind of microwave imaging radar, SAR images differ significantly from optical images. Previous research demonstrated that the real and imaginary components of low-resolution SAR complex images conform to Gaussian distributions while the image amplitude follows a Rayleigh distribution and the intensity follows a negative exponential distribution. This model applies well in textureless regions, such as agricultural areas and low-resolution sea clutter. However, as SAR resolution improves, the applicability of this model diminishes. Commonly used distributions to describe the amplitude and intensity of SAR images in real-world scenarios consist of the K-distribution, Weibull distribution, log-normal distribution, and gamma distribution.

Noncircularity and non-Gaussianity are commonly used statistical distribution information in BSS algorithms. The circularity is a unique statistic property for complex-valued signals, which reflects the symmetry of the signal distribution. A complex random variable z is called circular if its probability density function (PDF) satisfies, $\text{PDF}(ze^{j\theta}) = \text{PDF}(z) \quad \forall \theta \in \mathbb{R}$. Otherwise, it is noncircular. In fact, the second-order circularity is more commonly applied. If the pseudovariance of the zero-mean random variable is zero, then it is considered second-order circular. The normalized circularity coefficient (NCC) is a typical measurement for complex-valued signal circularity [33]

$$\text{NCC}(z) \triangleq \frac{\left| \text{E}(z^2) \right|}{\text{E}(|z|^2)}, \quad \text{NCC}(z) \in [0, 1] \tag{5}$$

where $\text{E}(\cdot)$ denotes the expectation operator, and $|\cdot|$ is the absolute value operator. $\text{NCC}(z) = 0$ means circularity, which infers that the PDF of a complex-valued random variable has the rotational invariance. The NCC of SAR echo signals closely relies on resolution, waveform parameters, and observed scene properties. For the SAR echo data, the sliding-average strategy is recommended to calculate the mean value in (5). Specifically, starting from the top left corner of the complex-valued SAR data matrix, a fixed-size rectangular window is used to select data and calculate the NCC of the selected data. Then, sliding averaging calculations are performed in both the azimuth and range directions with the sampling unit as the step size. By calculation, a new 2-D matrix can be obtained, with the elements of the matrix representing the NCC of each window-selected data. Typically, the new matrix is averaged along the azimuth or range dimension to obtain the variation of NCC along the other dimension. The size of the rectangular window for selecting data is empirically determined based on factors such as data resolution, with a typical value of 15×15 sampling units [34], [35].

The kurtosis is commonly used for non-Gaussianity description of real-valued random variables. Complex signals have three different types of fourth-order cumulants, which lead to three kinds of kurtosis measures for them. The most commonly applied kurtosis is [36]

$$\text{CSK}(z) \triangleq \mu_{2,2}(z) - 2 - |\mu_{2,0}(z)|^2 \tag{6}$$

where $\mu_{i,j}(z)$ is the normalized moments of z, specifically, $\mu_{2,2}(z) \triangleq \frac{\text{E}\{|z|^4\}}{\text{E}^2\{|z|^2\}}$, and $\mu_{2,0}(z)$ is exactly the normalized circularity coefficient $\text{NCC}(z)$. When $\text{CSK}(z) < 0$, it means sub-Gaussianity. $\text{CSK}(z) > 0$ means super-Gaussianity. $\text{CSK}(z) = 0$ infers that z obey the complex Gaussian distribution.

We analyzed a set of Sentinel-1 A SAR echo signals to assess their non-Gaussianity and noncircularity. The system used C-band linear frequency-modulated (LFM) signals for transmission and produced SAR images with a resolution of $5\text{ m} \times 5\text{ m}$. The selected scene contained diverse objects, such as bays, buildings, mountains, and sea waves. We evaluated the CSK and CC of the raw data, range compression (RC) data, and single look complex (SLC) data, as illustrated in Fig. 2.

From the previous figure, it can be observed that, for different scenes, the parameters of CSK and CC vary due to differences in scattering characteristics. In addition, the differences among raw data signals are small, followed by the RC data while the SLC data show the largest differences. Therefore, it can be concluded that there are differences in the non-Gaussianity and noncircularity of SAR echo signals from different types of targets, which provides the basis for the application of BSS algorithms on SAR data.

IV. IMPROVED ECHO SEPARATION STRATEGY

Based on the analysis earlier, the multichannel SAR echo data meet the prerequisites for using the ICA algorithm. Therefore, this separation method based on the statistical characteristics of the observed signals may be beneficial in improving the echo separation performance of practical multichannel SAR
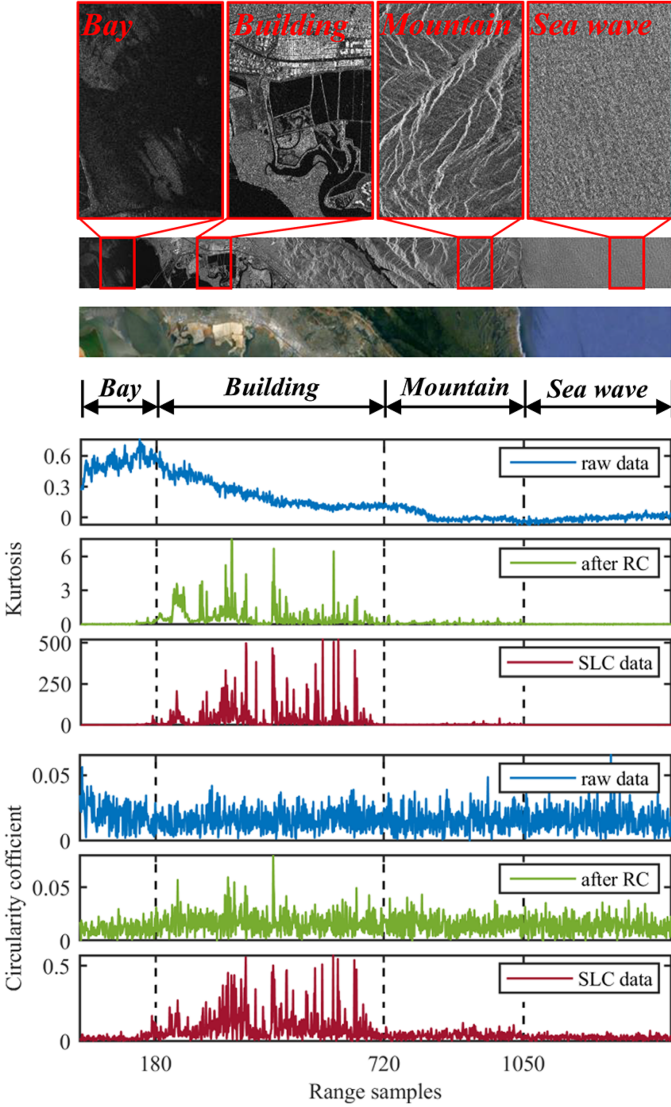
Fig. 2. Statistical analysis of SAR echo signals from different scatterers (Copernicus Sentinel data [2014]).

systems. This section will verify this idea using a wide-swath multitransmit multireceive SAR system.

A. Signal Model

A typical MIMO-SAR system is presented in Fig. 3. The antenna consists of M channels arranged uniformly in elevation and with the interchannel spacing of d. The strip-map SAR moves along the azimuth direction with a velocity of v at an altitude of H. In the slant range direction, the observed scene concludes N subswaths of the maximum unambiguous slant range width, $R_\mathrm{u} = \frac{2\mathrm{PRF}}{c}$, where PRF is the pulse repeat frequency, and c is the light speed. N adjacent channels of M transmit signals simultaneously to explore a single-range region, and all the channels are designed for signal reception. Due to the pulse sequence mechanism, echo signals from different regions are received at the same time, and alias in the time domain, which is described as (referenced to) range ambiguity.
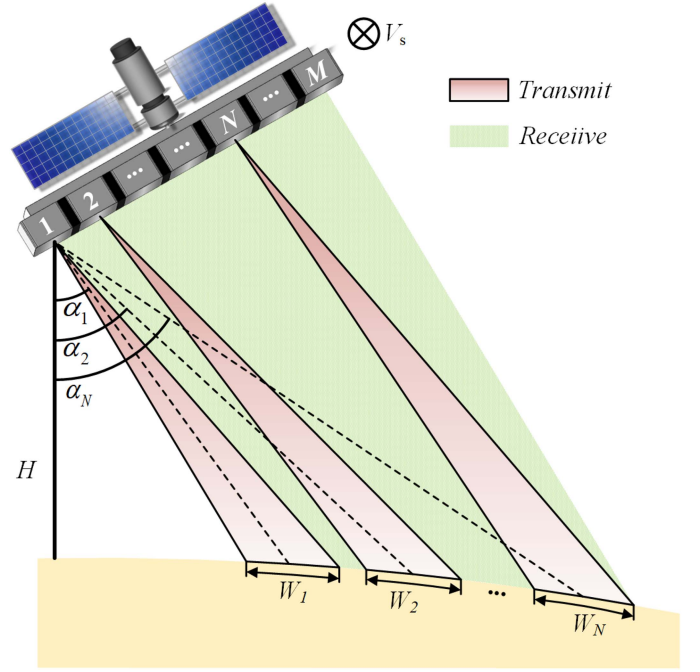

Fig. 3. Geometry of the wide-swath MIMO-SAR.

The waveform of the transmitted signals is the LFM pulse signal

$$x(\tau) = \mathrm{rect}\left(\frac{\tau}{T_\mathrm{r}}\right) \exp\left(\mathrm{j}\pi K_\mathrm{r}\tau^2\right) \exp\left(\mathrm{j}2\pi f_0\tau\right) \qquad (7)$$

where $\mathrm{rect}(\cdot)$ is the rectangular function, τ is the range time, T_r is the pulse duration, K_r is the chirp rate, and f_0 is the reference frequency.

When targets are apart with the distance positive multiples of R_u in the slant range, their round-trip propagation time would be positive multiples of the pulse repeat interval, resulting in echo signal aliasing in the time domain. Thus, taking the 1_st range region as a reference, for the m_th receiving channel, the echo signals of a target T in the n_th range region and its ambiguities can be yielded as

$$
\begin{aligned}
y_m(\tau, \eta) = \sum_{n=1}^{N} \xi_n &\cdot w_\mathrm{a}\left[\eta - (n-1)\Delta\eta - \eta_\mathrm{c}\right] \\
&\cdot w_\mathrm{r}(\tau - \Delta t_{n,m}) \\
&\cdot \exp\left[\mathrm{j}\pi K_\mathrm{r}(\tau - \Delta t_{n,m})^2\right] \\
&\cdot \exp\left(-\mathrm{j}2\pi f_0 \Delta t_{n,m}\right)
\end{aligned}
\qquad (8)
$$

where ξ_n is the complex coefficient (includes the back-scattering coefficient and the range attenuation coefficient), $w_\mathrm{a}(\eta)$ and $w_\mathrm{r}(\eta)$ are, respectively, denotes the azimuth and range signal amplitude, η is the azimuth time, η_c is the beam center cross time, $\Delta\eta$ is the pulse repeat interval, and $\Delta t_{n,m}$ denotes the round-trip time of the signal transmitted by the n_th channel and received by the m_th channel. $\Delta t_{n,m}$ is expressed in detail as

$$\Delta t_{n,m} = \frac{R_n^\mathrm{T}\left[\eta - (n-1)\Delta\eta\right] + R_{n,m}^\mathrm{R}(\eta)}{c}$$

$$= \frac{R_n^{\mathrm{T}}\left[\eta - (n-1)\Delta\eta\right] + R_{n,\mathrm{ref}}^{\mathrm{R}}(\eta)}{c}$$
$$+ \frac{\Delta R_{n,m}^{\mathrm{R}}(\eta)}{c} \tag{9}$$

where $R_n^{\mathrm{T}}(\eta)$ and $R_{n,m}^{\mathrm{R}}(\eta)$ are, respectively, the transmission and reception slant range, $R_{n,\mathrm{ref}}^{\mathrm{R}}(\eta)$ is the reference receiving slant range, and $\Delta R_{n,m}^{\mathrm{R}}(\eta)$ denotes the slant range difference between the receiving channels and the reference one.

One should note that for the signal amplitude and the LFM phase terms, $\Delta t_{n,m}$ can be approximated to $\Delta t_{1,1}$. That is to say, the influence of channel position on the two terms can be ignored. Thus, (8) can be further deduced as

$$y_m(\tau,\eta) = \sum_{n=1}^{N} \xi_n \cdot w_{\mathrm{a}}\left[\eta - (n-1)\Delta\eta - \eta_{\mathrm{c}}\right] \cdot w_{\mathrm{r}}(\tau - \Delta t_{1,1})$$
$$\cdot \exp\left[\mathrm{j}\pi K_{\mathrm{r}}(\tau - \Delta t_{1,1})^2\right]$$
$$\cdot \exp\left\{-\mathrm{j}\frac{2\pi f_0\left[R_n^{\mathrm{T}}(\eta - (n-1)\Delta\eta) + R_{n,\mathrm{ref}}^{\mathrm{R}}(\eta)\right]}{c}\right\}$$
$$\cdot \exp\left[-\mathrm{j}\frac{2\pi f_0\Delta R_{n,m}^{\mathrm{R}}(\eta)}{c}\right]$$
$$= \sum_{n=1}^{N} s_n(\tau,\eta) \cdot \exp\left[-\mathrm{j}\frac{2\pi f_0\Delta R_{n,m}^{\mathrm{R}}(\eta)}{c}\right] \tag{10}$$

where $s_n(\tau,\eta)$ is the traditional SAR signal model. The earlier equation can be rewritten in vector form as

$$\boldsymbol{y}(\tau,\eta) = \boldsymbol{A}(\eta) \cdot \boldsymbol{s}(\tau,\eta) \tag{11}$$

where $\boldsymbol{y}(\tau,\eta)$ is the received signal vector, $\boldsymbol{s}(\tau,\eta)$ is the source signal vector, and $\boldsymbol{A}(\eta)$ denotes the receiving array response matrix. They can be expressed as

$$\begin{cases} \boldsymbol{y}(\tau,\eta) \in \mathbb{C}^{M\times 1}, & [\boldsymbol{y}(\tau,\eta)]_{m,1} = y_m(\tau,\eta) \\ \boldsymbol{s}(\tau,\eta) \in \mathbb{C}^{N\times 1}, & [\boldsymbol{s}(\tau,\eta)]_{n,1} = s_n(\tau,\eta) \\ \boldsymbol{A}(\eta) \in \mathbb{C}^{M\times N}, & [\boldsymbol{A}(\eta)]_{m,n} = \exp\left[-\mathrm{j}\frac{2\pi f_0\Delta R_{n,m}^{\mathrm{R}}(\eta)}{c}\right]. \end{cases} \tag{12}$$

Under the far-field geometry and narrow-band signal assumption, one can regard the echo signals as plane waves. The slant range difference can be drawn as

$$\Delta R_{n,m}^{\mathrm{R}}(\eta) \approx (m-1)d\sin[\alpha_n(\eta) - \alpha_i] \tag{13}$$

where $\alpha_n(\eta)$ is the off-nadir angle, and α_i is the antenna array installation angle.

In practice, channel errors are thorny challenges for the coherent processing of multichannel signals. Here, we consider the channel errors consisting of amplitude error, phase error, range synchronous time error, and unexpected channel position variation. The amplitude error and phase error refer to the differences caused by the hardware characteristics of different channels, the temperature changes of the antenna array, etc. The range synchronous time error refers to the delay difference or clock asynchrony caused by the difference in transmission

cables and sampling hardware, and so on. This will introduce signal envelope offsets, linear phases, and constant phases in the signals. At the transmitter, the synchronous time error can be accurately precompensated, whereas at the receiver, it is usually compensated by the signal cross-correlation processing. The channel position variation refers to the physical position change caused by the antenna attitude change and the antenna deformation. It will cause the synchronous time error and constant phase error. In summary, the error model can be established as the constant amplitude error, constant phase error, and linear phase error between channels. Therefore, without loss of generality, the receiving echo signals considering channel errors can be rewritten as

$$\widetilde{\boldsymbol{y}}(\tau,\eta) = \boldsymbol{E} \odot \boldsymbol{P}(\tau) \odot \boldsymbol{A}(\eta) \cdot \boldsymbol{s}(\tau,\eta) \tag{14}$$

where $\boldsymbol{E}$ is the constant error matrix, $\boldsymbol{P}(\tau)$ is the linear phase error matrix, and $\odot$ denotes the Hadamard product. As above, the error matrix is further as

$$\begin{cases} \boldsymbol{E} \in \mathbb{C}^{M\times N}, & [\boldsymbol{E}]_{m,n} = a_{m,n} \cdot \exp\left\{\mathrm{j}p_{m,n}\right\} \\ \boldsymbol{P}(\tau) \in \mathbb{C}^{M\times N}, & [\boldsymbol{P}(\tau)]_{m,n} = \exp\left\{\mathrm{j}q_{m,n}\tau\right\} \end{cases} \tag{15}$$

where $a_{m,n}$ and $p_{m,n}$, respectively, denotes the amplitude and phase error, and $q_{m,n}$ is the coefficient of linear phase error. By combining the error matrices and the mixing matrix, (14) is rewritten as

$$\widetilde{\boldsymbol{y}}(\tau,\eta) = \widetilde{\boldsymbol{A}}(\tau,\eta) \cdot \boldsymbol{s}(\tau,\eta). \tag{16}$$

Equation (16) describes the aliasing process of different region echo signals at the reception end, and the mixing matrix is the Hadamard product of the error matrix and the receiving the array response matrix.

B. Echo Signal Separation

The signal model with errors has been obtained in the previous section, and the separation scheme of the echo signal will be given in this section.

From Section III, one can see that after RC of SAR data, the difference in noncircularity and non-Gaussianity among different scatters is greater. Thus, the RC is conducted as the first step to enhance the difference. Besides, the cross-correlation processing is conducted to calibrate large synchronous time errors. One should note that these two procedures are optional for the complete framework. In the situation of large differences among mixed SAR data and small system errors, they can be omitted.

1) Compensation for Time Dependence and Spatial Dependence of Mixing Matrix: From (16), one can see that the echo signals considering errors do not match the linear instantaneously mixing model for time dependence and spatial dependence of the mixing matrix. The time dependence refers to $\widetilde{\boldsymbol{A}}(\tau,\eta)$ depending on the azimuth time η and the range time τ. The spatial dependence refers to $\widetilde{\boldsymbol{A}}(\tau,\eta)$ varying with the range.

Actually, the azimuth time dependence of the mixing matrix is similar to the aperture extension loss (AEL) problem faced by
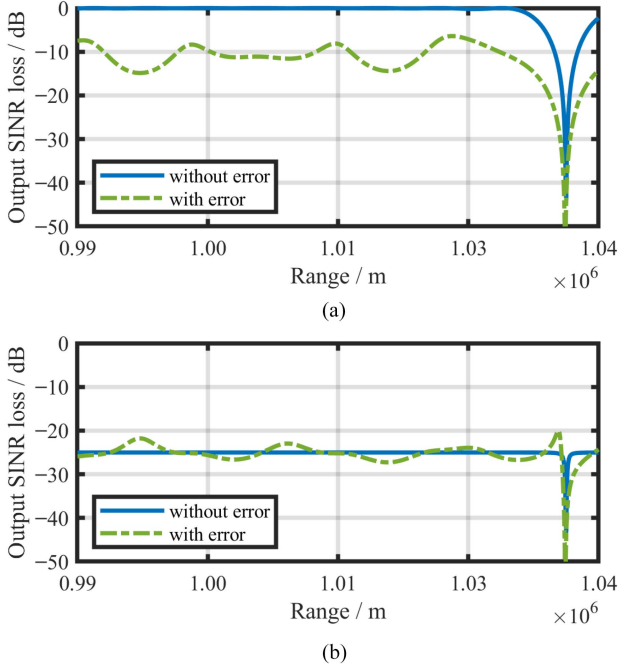
Fig. 4. Output SINR loss of LCMV and PDC-LCMV. Channel error is constant phase error following normal distribution along channels, with expectation as 0 and variance as $(\pi/36)^2$. (a) LCMV with null constraints. (b) PDC-LCMV with constant constraints.

conventional digital beamforming SAR [32]. Generally, it is usually negligible, whereas, in the case of high azimuth resolution, the AEL can be compensated in range–Doppler domain. This problem is not discussed in detail in this article. The range time dependence can be compensated by simple cross-correlation of signals between channels.

As for the spatial dependence, it is explained as $\widetilde{\boldsymbol{A}}(\tau, \eta)$ being related to the elevation angle, which directly depends on the range position of scatterers. An effective solution is dividing the range dimension into blocks. One can regard the mixing matrix constant within a block.

Another method is adopting a modified LCMV beamformer. Based on (2), we modify the constraint vector to $\boldsymbol{e}' = [1, \beta \mathbf{1}^{1\times(N-1)}]^{\mathrm{H}}$, where $0 < \beta < 1$ is a constant. Under the channel errors, the null constraints are replaced with constant constraints to improve the beamformer's stationarity over the range position. We call it a pure-decimal-constraint LCMV (PDC-LCMV) beamformer. Fig. 4 gives the results of output SINR loss of LCMV and PDC-LCMV changing with the mainlobe steering direction, with a null or constant constraint in the range far field. When the constant constraint is applied, the SINR loss is more stable with errors. Thus, despite the beamformer does not remove the ambiguities with nulls, it yields a range-unvarying linearity between the expected signal and ambiguities. After the earlier processing, the echo is

$$\widetilde{\boldsymbol{y}}(\tau, \eta) = \widetilde{\boldsymbol{A}} \cdot \boldsymbol{s}(\tau, \eta). \tag{17}$$

2) Echo Separation With Statistical Characteristics: ICA is a solution for the BSS problem, which aims to optimally extract the source signals from the mixed signals based on signal

independence. According to (4), the signal model (17) needs to be reshaped to fit the linear instantaneous signal mixture model. Before further processing, the 2-D data matrix should be reordered to a 1-D one long-range direction, which is

$$\widetilde{\boldsymbol{y}}(k) = \widetilde{\boldsymbol{A}} \cdot \boldsymbol{s}(k), \quad k = 1, \ldots, N_a \times N_r \tag{18}$$

where k is the sample axis, and N_a and N_r are the azimuth and range size of the echo data matrix, respectively.

Generally, the ICA algorithm mainly focuses on two aspects: 1) establishing an objective function and 2) designing an optimization algorithm. The former depends on the choice of the independence criterion, which includes common criteria, such as mutual information minimization, entropy maximization, nonGaussianity maximization, and maximum likelihood. For an example, based on (4), the mutual information is

$$
\begin{aligned}
I(\widehat{\boldsymbol{s}}) &= \sum_{n=1}^{N} \mathcal{H}(\widehat{s}_n) - \mathcal{H}(\widehat{\boldsymbol{s}}) = \sum_{n=1}^{N} \mathcal{H}(\widehat{s}_n) \\
&\quad - 2\ln|\det(\boldsymbol{D})| - \mathcal{H}(\boldsymbol{y})
\end{aligned} \tag{19}
$$

where $\mathcal{H}(\cdot)$ is the differential entropy operator. The mutual information describes the correlation between the separated signals. The mutual-information-based ICA algorithm can be simply described as finding a separation matrix $\boldsymbol{D}$ that minimizes the mutual information of the separated signals. One can see that the mutual information involves the entropy of the complex random variables. According to the probability density function of a complex random variable, the entropy can describe both non-Gaussianity and noncircularity. Based on this, Li et al. [37] proposed an excellent complex entropy-bound minimization (EBM) algorithm. The algorithm selects a separation vector $\boldsymbol{d}_n$ (for one single-source signal) in $\boldsymbol{D}$ as the optimization objective keeps the rest ones $\boldsymbol{d}_i, \quad i = 1, 2, \ldots, n-1, n+1, \ldots, N$ unchanged and obtains the separation vector of each source signal in series. The specific optimization model is as follows:

$$
\begin{cases}
\min_{\boldsymbol{d}_n} & \widehat{\mathcal{H}}(\widehat{s}_n) - 2\ln|\boldsymbol{h}_n^{\mathrm{H}} \boldsymbol{d}_n| \\
\text{s.t.} & \|\boldsymbol{d}_n\| = 1
\end{cases} \tag{20}
$$

where $\widehat{\mathcal{H}}(\widehat{s}_n)$ is the entropy bound and $\boldsymbol{h}_n$ is the orthogonal vector of $\boldsymbol{d}_n$. The constraint $\|\boldsymbol{d}_n\| = 1$ limits the source signal variance to 1, which can be achieved by whitening preprocessing. It is usually impossible to obtain the accurate entropy in practice. Therefore, the EBM introduces two types of entropy bounds based on the maximum entropy distribution optimization model, using linear decomposition and polar decomposition, which correspond to the weighted linear combination distribution family and the elliptical distribution family, respectively, so that the maximum entropy of a wide range of binary distribution signals can be estimated. The two types of entropy bounds corresponding to the two decompositions are [37]

$$
\begin{cases}
\mathcal{H}^{\mathrm{I}}(\widehat{s}_n) = \ln[\det(\boldsymbol{B})] + 2\mathcal{H}(y_g) \\
\quad - \mathrm{J}\{\mathrm{E}[G_{k_1}^{\mathrm{I}}(u)]\} - \mathrm{J}\{\mathrm{E}[G_{k_2}^{\mathrm{I}}(v)]\}, \\
\quad [\mathcal{R}(\widehat{s}_n), \mathcal{I}(\widehat{s}_n)]^{\mathrm{T}} = \boldsymbol{B}[u, v]^{\mathrm{T}} \\
\mathcal{H}^{\mathrm{II}}(\widehat{s}_n) = \ln[\det(\boldsymbol{B})] + 2\mathcal{H}(y_g) \\
\quad - \mathrm{J}\{\mathrm{E}[G_l^{\mathrm{II}}(r)]\}, \\
\quad [\mathcal{R}(\widehat{s}_n), \mathcal{I}(\widehat{s}_n)]^{\mathrm{T}} = \boldsymbol{B}r[\cos(\theta), \sin(\theta)]^{\mathrm{T}}
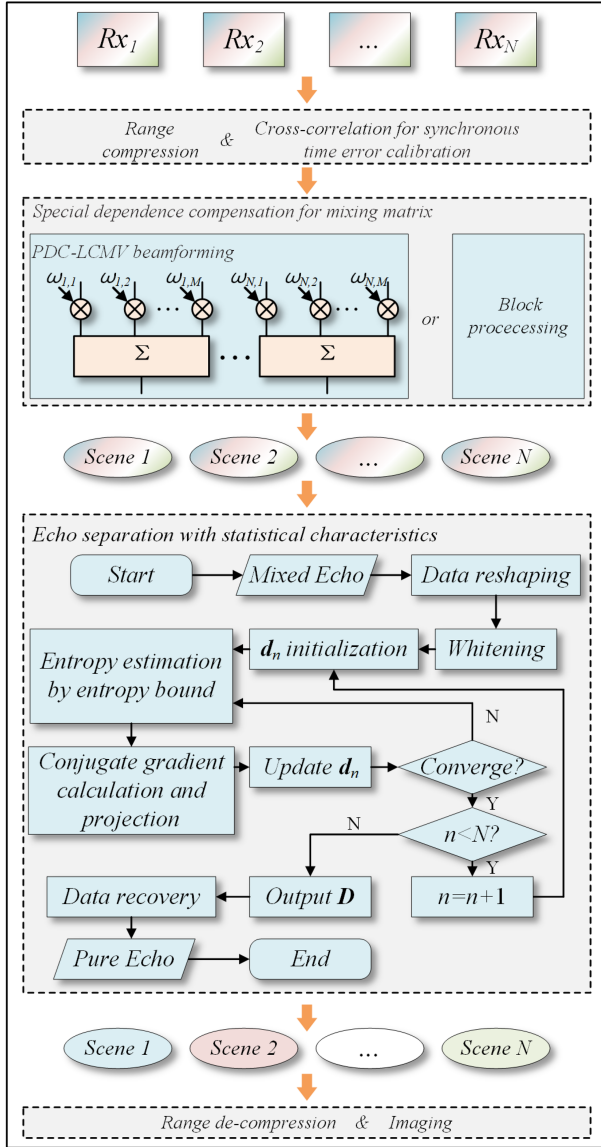\end{cases} \tag{21}
$$

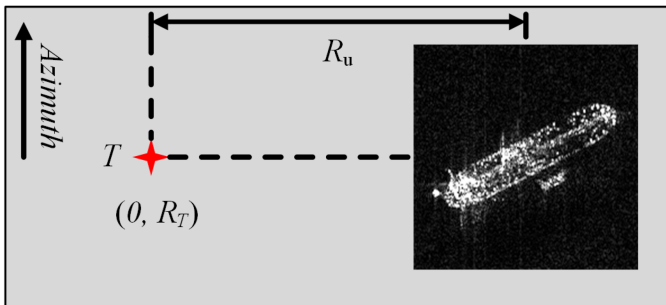Fig. 5.   Flowchart of the proposed scheme.

Fig. 6.   Geometry of the point-target simulation experiment.

where $\boldsymbol{B}$ is a two-order nonsingular square matrix and $\mathcal{H}(y_g) = \frac{1}{2}\ln(2\pi e)$ is the entropy of the standard normal distribution. $J(\cdot)$ is the negative entropy operator. $G_k^{\mathrm{I}}, k = 1, 2, \ldots, K$ and $G_l^{\mathrm{II}}, l = 1, 2, \ldots, L$ (containing K and L basic measurement

functions, respectively) represent two groups of basic measurement functions corresponding to the two decompositions. By performing QR decomposition analysis on the matrix $\boldsymbol{B}$ and solving the negative entropy according to the specific measurement function, the explicit expressions of the two types of entropy bounds can be further obtained. According to the maximum likelihood criterion, the tightest one among the entropy bounds corresponding to all measurement functions is selected as $\widehat{\mathcal{H}}(\widehat{s}_n)$.

Then, EBM performs a line search optimization to get the updating separation vector

$$\begin{cases} \boldsymbol{d}_n^+ = \boldsymbol{d}_n - \beta \frac{\triangledown - \mathcal{R}\{\boldsymbol{d}_n^{\mathrm{H}}\triangledown\}\boldsymbol{d}_n}{\|\triangledown - \mathcal{R}\{\boldsymbol{d}_n^{\mathrm{H}}\triangledown\}\boldsymbol{d}_n\|} \\ \boldsymbol{d}_n^{\mathrm{new}} = \frac{\boldsymbol{d}_n^+}{\|\boldsymbol{d}_n^+\|} \end{cases} \tag{22}$$

where β is the iteration step size, and $\triangledown$ is the conjugate gradient of the objective function in (20). In summary, the basic process of estimating the separation matrix based on the EBM algorithm is as follows. First, one should initialize $\boldsymbol{D}$, which can be achieved with the ideal LCMV weighting vector. Second, a projection conjugate gradient iterative algorithm is used to find the optimal separation weighted vector $\boldsymbol{d}_n$ for each source signal. The iterative criterion is to minimize the mutual information of the output signals, which is calculated through the concept of entropy bounds.

The EBM algorithm has excellent performance for complex signals. The two types of entropy estimators used can accurately estimate the entropy of a wide range of binary distribution signals. It utilizes both the noncircularity and non-Gaussianity of the signals and can adapt to various complex distributions. Other complex ICA algorithms based on similar principles can also be applied here.

After separation, one gets N 1-D signals corresponding to N range regions. One should restore them to 2-D. The restored signals can be used for conventional imaging processing.

From the perspective of degrees of freedom, in the previous model, the number of receiving channels in the system is greater than or equal to the number of transmitting ones. When $M < N$, the algorithm needs improvement to deal with an underdetermined model.

To sum up, the processing process of echo separation with statistical characteristics is as follows.

1) Reshaping the 2-D signal model (17) to 1-D vectors.
2) Whitening the data.
3) Initializing the separation vector $\boldsymbol{d}_n$.
4) Calculating $\boldsymbol{h}_n$ orthogonal to $\boldsymbol{d}_i, i = 1, 2, \ldots, n - 1, n + 1, \ldots, N$.
5) Separating the signals with $\boldsymbol{d}_n$ and estimating the entropy with two types of entropy estimators [37]. Select the tightest ones as the entropy-bound estimations.
6) According to the entropy-bound estimations and $\boldsymbol{h}_n$, calculating the projection conjugate gradient of the objective function in (20) and updating $\boldsymbol{d}_n$ with (22).
7) Repeating steps 4–6 until convergence (usually limit the number of iterations to 300).
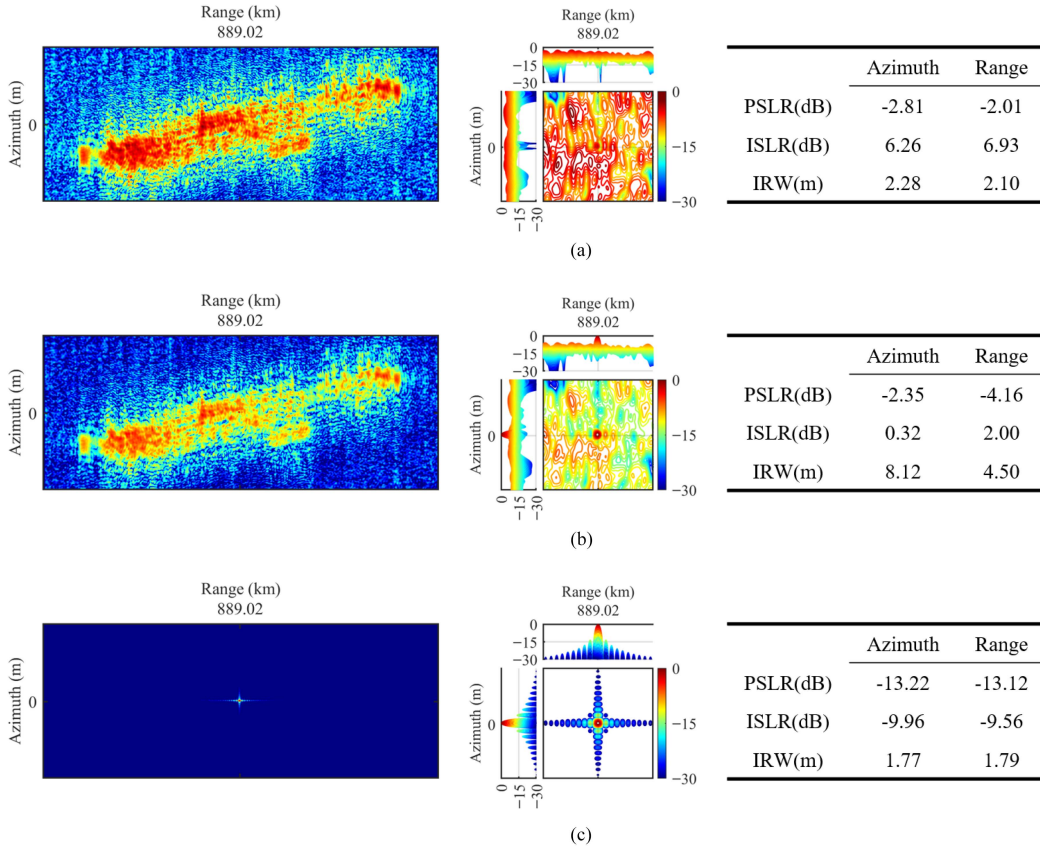8) $n = n + 1$, Repeating steps 3–7 until $n = N$.

Fig. 7. Results of the point-target simulation experiment. (a) Original mixed signal. (b) Biased LCMV processed signal. (c) Proposed scheme processed signal.

9) Outputting D and separating the signals.

10) Recovering the data to 2-D matrices.

After separating, the SAR echo signals are further used for imaging. The complete processing flowchart is as Fig. 5.

The key steps of the proposed scheme include the spatial dependence compensation for the mixing matrix and the ICA algorithm processing. Typically, the former is achieved by PDC-LCMV beamforming, and the latter is by the EBM algorithm. Next, we will discuss the computational complexity of these two steps. Assuming the SAR data dimension is $N_a \times N_r \times N$ (azimuth $times$ range $times$ receiving channels), the computational complexity of the PDC-LCMV is $O(N_r M N^3 + N_r N^4 + N_a M N_r N)$. As for the EBM algorithm, the computational complexity is $O(N_a N_r N^2 T)$, where T is the number of iterations. Thus, the total computational complexity of the proposed scheme can be approximated to the sum of the above two ones. As for the traditional LCMV beamforming for range ambiguity separation, it has a similar processing as the PDC-LCMV. Thus, it can be considered that compared to the traditional LCMV algorithm, the proposed scheme has increased computational complexity, where the increase is attributed to the EBM algorithm section. In terms of hardware resources for SAR systems, the proposed scheme does not require any additional hardware.

It can be seen that T, N_a, and N_r are the primary factors affecting the efficiency of the proposed method. The former is typically necessary to ensure the separation effect. Therefore, one can consider selecting a small block from the SAR data

TABLE I
SIMULATION PARAMETERS

Parameter	Value
Platform height	710 km
Platform velocity	7503 m/s
Off-nadir angle (center of the first region)	37°
Carrier frequency	9.6 GHz
Signal bandwidth	75 MHz
Pulse duration	10 μs
PRF	4640 Hz
Maximum unambiguous slant range width	32.33 km
Size of antenna (azimuth $\times$ elevation)	4 m $\times$ 2 m
Number of channels (transmit $\times$ receive)	2 $\times$ 2

matrix as the processing subject to reduce the processing time of the proposed scheme. In the experiments of this article, the complete SAR data matrices are used for processing.

V. SIMULATION EXPERIMENTS

A. Point-Target Simulation

In order to verify the effectiveness of the above proposal, we conducted a point-target simulation experiment. The experimental parameters are shown in Table I. The observed scenario consists of a near-field point target and a far-field ship target, with a maximum unambiguous slant range width of R_u between
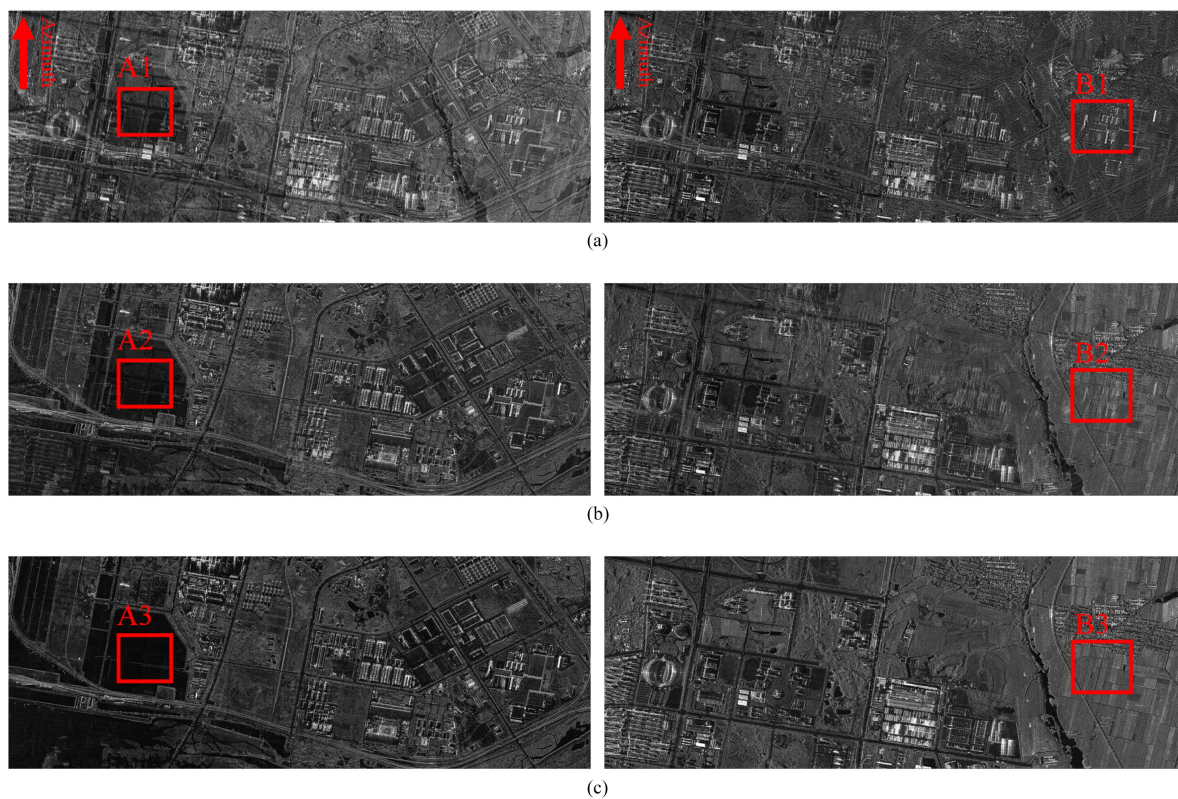
Fig. 8. Distributed scatterer simulation experiment results of the near-field (left) and far-field (right) areas. (a) Original mixed signal. (b) Biased LCMV processed signal. (c) Proposed scheme processed signal.
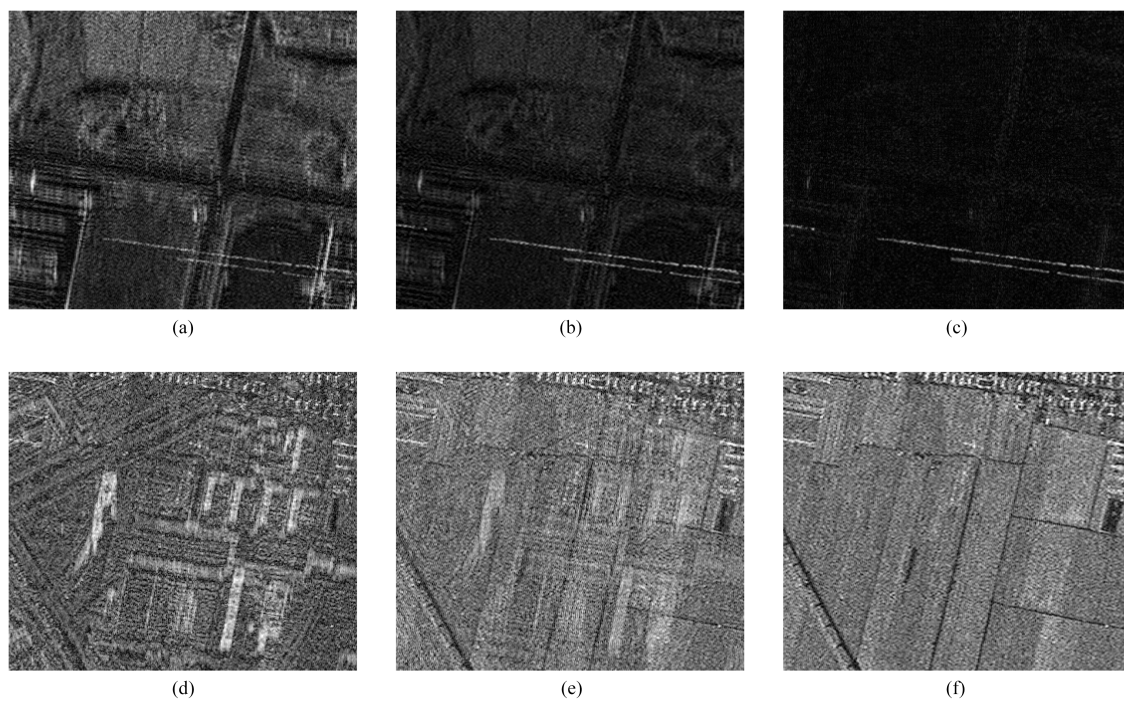

Fig. 9. Enlarged views of areas A1–A3 and B1–B3. (a) A1. (b) A2. (c) A3. (d) B1. (e) B2. (f) B3.
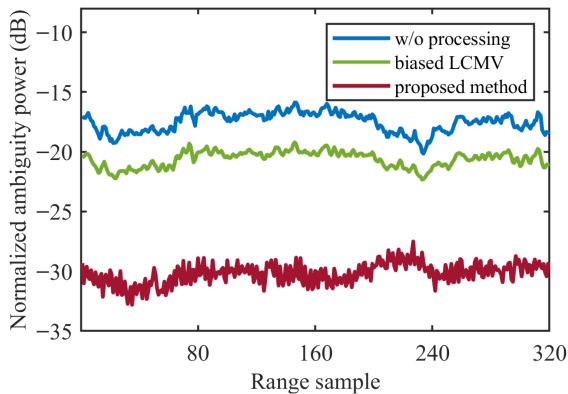
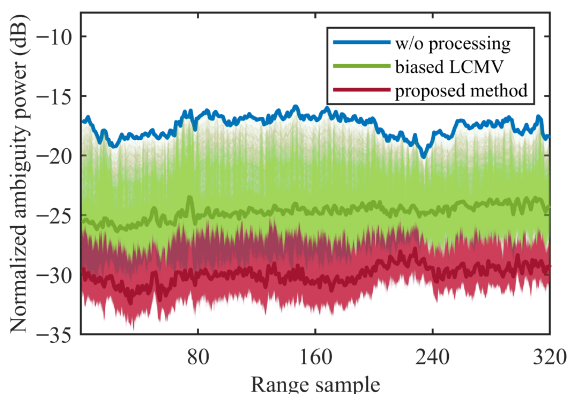Fig. 10. Normalized ambiguity power of area A.

Fig. 11. Normalized ambiguity power of area A of 10000 experiments.

B. Distributed Scatterer Simulation

For further verification, based on the system parameters in Table I, a distributed target simulation is designed in this section. Two GF-3 SAR images with a resolution of 1 m are considered as two range regions of a distance of R_u. The simulation results are shown in the following.

Similar to the point-target simulation, severe ambiguities appear in the imaging results of single-channel echo without processing [see Fig. 8(a)]. Through biased LCMV beamforming, the ambiguities are both mitigated [see Fig. 8(b)]. The proposed method further suppresses the ambiguity energy [see Fig. 8(c)]. Fig. 9 gives the enlarged slices of two areas for clarity. For quantitative analysis, a water area (A1–A3) in the first region is selected to calculate the normalized ambiguity power as Fig. 10. Under the conditions of no processing, biased LCMV processing, and the processing proposed, the normalized ambiguity power (NAP) is -17 dB, -20 dB, and -30 dB, respectively.

Actual channel errors are usually random. To avoid specific circumstances, we conducted 10 000 Monte Carlo experiments. In these experiments, we randomly generated channel errors according to a Gaussian distribution, then processed the data using three different methods, and finally calculated the NAP. The results are shown in Fig. 11.

The semitransparent lines represent each experiment result while the solid lines indicate the average values. Due to the random alterations in the null and main-lobe direction of the LCMV beam pattern caused by the random channel errors, there is a considerable variation in the results of the biased LCMV beamforming, with the NAP changing between -17 and -30 dB. The NAP of the proposed method concentrates between -27 and -33 dB, demonstrating good robustness. Therefore, it can be concluded that the proposed method effectively addresses channel errors. Compared to the traditional LCMV approach, the proposed method has better separation of signal and ambiguity, and the algorithm is more stable.

VI. DISCUSSION

Through theoretical analysis and experiments above, the main advantages of the proposed method are mainly in four aspects. First, it can be used to alleviate the problem of null-steering beamformer mismatch caused by channel errors. Second, when the number of channels (observation dimensions) is small, mere null-steering beamforming processing becomes more sensitive to channel errors while the proposed method is even applicable in cases where the channel number is equal to the source number. Third, in addition to channel errors, the proposed method can also cope with separation failure caused by terrain fluctuations and orbit errors to a certain extent. Fourth, the proposed method does not require any additional hardware resources.

Essentially, the scheme proposed in this article no longer starts from the system but from the statistical characteristics of the observed scene, adding an additional dimension to the processing and utilizing signal independence for separation. Therefore, the efficacy of this scheme depends to some extent on the observed scene. When source signals come from objects with

the two scenarios, as shown in Fig. 6. Channel errors include amplitude error (expectation 0 dB and variance -18 dB), phase error (expectation 0 rad and variance $(\pi/36)^2$ rad), and synchronous time error (expectation 0 ns and variance 1 ns^2). They all follow the normal distribution along channels. Due to the pulse waveform scheme of SAR, we expect that the near-field point will be aliased with the echoes of the far-field ship. Fig. 7 shows the imaging results of the mixed echoes, the biased LCMV (with channel errors) processed data, and the results obtained using the proposed method. The impact of the antenna pattern is not considered in the simulation for a convincing result display.

Fig. 7(a) shows the original mixed echo imaging result, where the point target is submerged in the ambiguities of the ship and is even unrecognizable. In Fig. 7(b), due to channel errors, there is a bias in the LCMV filtering. The ambiguities in the image are somewhat alleviated. However, there are still residual ambiguities of approximately -10 dB around the point target. After applying the proposed method, the ambiguities are suppressed to below -30 dB. Moreover, the point is well focused after processing [se Fig. 7(c)]. Therefore, one can say that, first, the proposed method effectively separates the expected signals and ambiguities. Second, the proposed method does not affect the imaging performance.

similar scattering characteristics and roughness, the scheme performance may degrade. However, this situation usually occurs in ocean mapping situations, which is not common.

Although the derivation in this article is based on a wide-swath MIMO-SAR system with the observation channels equal to the number of the range regions, the proposed scheme is actually applicable to any system with the number of source signals less than or equal to the observation dimensions. Furthermore, it is applicable to various echo separation requirements based on multichannel receiving systems. In addition to separating range ambiguity signals, this scheme is also applicable to separating SAR signals from interference signals, and so on.

VII. CONCLUSION

High-resolution wide-swath SAR imaging system is of great significance for remote sensing mapping. The null-steering beamforming technology is widely used in such systems, which, however, is highly susceptible to channel errors. This article proposes an echo separation scheme based on the statistical characteristics of SAR echoes to mitigate residual channel errors encountered during practical processing. First, a linear instantaneous mixture model of source signals is constructed through a quasi-LCMV beamforming approach. Subsequently, an advanced complex ICA algorithm, EBM, is employed to separate the source signals by leveraging their independence. Theoretical derivations, simulation experiments, and comparative analysis lead to the following conclusions. Compared to simple null-steering beamforming, the proposed scheme significantly enhances echo separation performance in realistic error environments, eliminating the need for additional hardware resources, and offering robustness particularly when the number of channels is limited. Simulation experiment results demonstrate that traditional null-steering beamforming exhibits highly unstable variations in ambiguity gain across a wide dynamic range. Further applying the proposed method, ambiguity power is consistently suppressed at a lower level, resulting in a robust performance characterized by reduced ambiguity. Therefore, the proposed method effectively alleviates the channel error issue in multichannel SAR systems, ensuring its high-resolution wide-swath imaging performance.

REFERENCES

[1] A. Moreira, P. Prats-Iraola, M. Younis, G. Krieger, I. Hajnsek, and K. P. Papathanassiou, "A tutorial on synthetic aperture radar," *IEEE Geosci. Remote Sens. Mag.*, vol. 1, no. 1, pp. 6–43, Mar. 2013.

[2] K. Tomiyasu, "Tutorial review of synthetic-aperture radar (SAR) with applications to imaging of the ocean surface," *Proc. IEEE*, vol. 66, no. 5, pp. 563–583, May 1978.

[3] N. Gebert, G. Krieger, and A. Moreira, "Multi-channel ScanSAR for high-resolution ultra-wide-swath imaging," in *Proc. 7th Eur. Conf. Synthetic Aperture Radar*, 2008, pp. 1–4.

[4] M. Villano, G. Krieger, and A. Moreira, "Onboard processing for data volume reduction in high-resolution wide-swath SAR," *IEEE Geosci. Remote Sens. Lett.*, vol. 13, no. 8, pp. 1173–1177, Aug. 2016.

[5] M. Younis, F. Bordoni, N. Gebert, and G. Krieger, "Smart multi-aperture radar techniques for spaceborne remote sensing," in *Proc. IEEE Int. Geosci. Remote Sens. Symp.*, 2008, vol. 3, pp. III-278–III-281.

[6] A. Currie and M. A. Brown, "Wide-swath SAR," *Proc. Inst. Elect. Eng. F (Radar Signal Process.)*, vol. 139, no. 2, pp. 122–135, 1992.

[7] G. Krieger, N. Gebert, and A. Moreira, "Unambiguous SAR signal reconstruction from nonuniform displaced phase center sampling," *IEEE Geosci. Remote Sens. Lett.*, vol. 1, no. 4, pp. 260–264, Oct. 2004.

[8] F. Feng, S. Li, W. Yu, and S. Wang, "Study on the processing scheme for space–time waveform encoding SAR system based on two-dimensional digital beamforming," *IEEE Trans. Geosci. Remote Sens.*, vol. 50, no. 3, pp. 910–932, Mar. 2012.

[9] F. Feng, S. Li, W. Yu, P. Huang, and W. Xu, "Echo separation in multidimensional waveform encoding SAR remote sensing using an advanced null-steering beamformer," *IEEE Trans. Geosci. Remote Sens.*, vol. 50, no. 10, pp. 4157–4172, Oct. 2012.

[10] G. D. Callaghan and I. D. Longstaff, "Wide-swath space-borne SAR using a quad-element array," *Proc. Inst. Elect. Eng. (Radar, Sonar, Navigation)*, vol. 146, no. 3, pp. 159–165, 1999.

[11] M. Suess, B. Grafmueller, and R. Zahn, "A novel high resolution, wide swath SAR system," in *Proc. Scanning Present Resolving Future Proc. IEEE Int. Geosci. Remote Sens. Symp.*, 2001, vol. 3, pp. 1013–1015.

[12] F. He, X. Ma, Z. Dong, and D. Liang, "Digital beamforming on receive in elevation for multidimensional waveform encoding SAR sensing," *IEEE Geosci. Remote Sens. Lett.*, vol. 11, no. 12, pp. 2173–2177, Dec. 2014.

[13] M. Villano, G. Krieger, and A. Moreira, "Waveform-encoded SAR: A novel concept for nadir echo and range ambiguity suppression," in *Proc. 12th Eur. Conf. Synthetic Aperture Radar*, 2018, pp. 1–6.

[14] W.-Q. Wang, "Mitigating range ambiguities in high-PRF SAR with OFDM waveform diversity," *IEEE Geosci. Remote Sens. Lett.*, vol. 10, no. 1, pp. 101–105, Jan. 2013.

[15] X. He, G. Liao, S. Zhu, J. Xu, and J. Zhu, "Range ambiguous clutter suppression approach with elevation time diverse array," *IEEE Trans. Aerosp. Electron. Syst.*, vol. 58, no. 1, pp. 359–373, Feb. 2022.

[16] Z. Lv, H. Fan, Z. Chen, J. Qiu, M. Ren, and Z. Zhang, "Mitigate the LFM-PRFI in SAR data: Joint down-range and cross-range filtering," *IEEE Trans. Geosci. Remote Sens.*, vol. 61, Apr. 2023, Art. no. 5205918.

[17] G. Krieger, "MIMO-SAR: Opportunities and pitfalls," *IEEE Trans. Geosci. Remote Sens.*, vol. 52, no. 5, pp. 2628–2645, May 2014.

[18] W.-Q. Wang and J. Cai, "MIMO SAR using chirp diverse waveform for wide-swath remote sensing," *IEEE Trans. Aerosp. Electron. Syst.*, vol. 48, no. 4, pp. 3171–3185, Oct. 2012.

[19] J. Xu, G. Liao, and H. C. So, "Space-time adaptive processing with vertical frequency diverse array for range-ambiguous clutter suppression," *IEEE Trans. Geosci. Remote Sens.*, vol. 54, no. 9, pp. 5352–5364, Sep. 2016.

[20] H. Huang et al., "A novel channel errors calibration algorithm for multichannel high-resolution and wide-swath SAR imaging," *IEEE Trans. Geosci. Remote Sens.*, vol. 60, Feb. 2021, Art. no. 5201619.

[21] Y.-Y. Liu, Z.-F. Li, Z.-Y. Suo, and Z. Bao, "A novel channel phase bias estimation method for spaceborne along-track multi-channel HRWS SAR in time-domain," in *Proc. IET Int. Radar Conf.* 2013, pp. 1–4.

[22] L. Zhang, M.-D. Xing, C.-W. Qiu, and Z. Bao, "Adaptive two-step calibration for high-resolution and wide-swath SAR imaging," *IET Radar, Sonar, Navigation*, vol. 4, no. 4, pp. 548–559, 2010.

[23] T. Yang, Z. Li, Y. Liu, and Z. Bao, "Channel error estimation methods for multichannel SAR systems in azimuth," *IEEE Geosci. Remote Sens. Lett.*, vol. 10, no. 3, pp. 548–552, May 2013.

[24] Q. Zhao et al., "Echo separation for space-time waveform-encoding SAR with digital scalloped beamforming and adaptive multiple null-steering," *IEEE Geosci. Remote Sens. Lett.*, vol. 18, no. 1, pp. 92–96, Jan. 2021.

[25] H. Wang, Y. Zhang, J. Xu, G. Liao, and C. Zeng, "A novel range ambiguity resolving approach for high-resolution and wide-swath SAR imaging utilizing space-pulse phase coding," *Signal Process.*, vol. 168, 2020, Art. no. 107323.

[26] P. Dey, N. Trivedi, U. Satija, B. Ramkumar, and M. S. Manikandan, "Single channel blind source separation for MISO communication systems," in *Proc. IEEE 86th Veh. Technol. Conf.*, 2017, pp. 1–5.

[27] A. Belouchrani, K. Abed-Meraim, J.-F. Cardoso, and E. Moulines, "A blind source separation technique using second-order statistics," *IEEE Trans. Signal Process.*, vol. 45, no. 2, pp. 434–444, Feb. 1997.

[28] M. Pal, R. Roy, J. Basu, and M. S. Bepari, "Blind source separation: A review and analysis," in *Proc. Int. Conf. Oriental COCOSDA Held Jointly With Conf. Asian Spoken Lang. Res. Eval.*, 2013, pp. 1–5.

[29] L. Dominic, C. Sylvain, and G. Dominique, "An introduction to independent component analysis: Infomax and FastICA algorithms," *Tut. Quantitative Methods Psychol.*, vol. 6, no. 1, pp. 31–38, 2010.

[30] X. Geng, L. Ji, and K. Sun, "Principal skewness analysis: Algorithm and its application for multispectral/hyperspectral images indexing," *IEEE Geosci. Remote Sens. Lett.*, vol. 11, no. 10, pp. 1821–1825, Oct. 2014.

[31] S. Chen et al., "Multi-electromagnetic jamming countermeasure for airborne SAR based on maximum SNR blind source separation," *IEEE Trans. Geosci. Remote Sens.*, vol. 60, Dec. 2022, Art. no. 5240211.

[32] S. Chang, Y. Deng, Y. Zhang, Q. Zhao, R. Wang, and K. Zhang, "An advanced scheme for range ambiguity suppression of spaceborne SAR based on blind source separation," *IEEE Trans. Geosci. Remote Sens.*, vol. 60, Jun. 2022, Art. no. 5230112.

[33] E. Ollila, "On the circularity of a complex random variable," *IEEE Signal Process. Lett.*, vol. 15, pp. 841–844, Nov. 2008.

[34] X. Leng, K. Ji, S. Zhou, X. Xing, and H. Zou, "Discriminating ship from radio frequency interference based on noncircularity and non-Gaussianity in sentinel-1 SAR imagery," *IEEE Trans. Geosci. Remote Sens.*, vol. 57, no. 1, pp. 352–363, Jan. 2019.

[35] W. Wu, X. Li, H. Guo, L. Ferro-Famil, and L. Zhang, "Noncircularity parameters and their potential applications in UHR MMW SAR data sets," *IEEE Geosci. Remote Sens. Lett.*, vol. 13, no. 10, pp. 1547–1551, Oct. 2016.

[36] E. Ollila and V. Koivunen, "Adjusting the generalized likelihood ratio test of circularity robust to non-normality," in *Proc. IEEE 10th Workshop Signal Process. Adv. Wireless Commun.*, 2009, pp. 558–562.

[37] X.-L. Li and T. Adali, "Complex independent component analysis by entropy bound minimization," *IEEE Trans. Circuits Syst. I, Reg. Papers*, vol. 57, no. 7, pp. 1417–1430, Jul. 2010.

Xiangrui Meng received the B.S. degree in electronics information science and technology from Central South University, Changsha, China, in 2019. He is currently working toward the Ph.D. degree in communicaiton and information system with the University of Chinese Academy of Sciences, Beijing, China, and also with the Aerospace Information Research Institute, Chinese Academy of Sciences.

His scientific interest includes synthetic aperture radar remote sensing, focusing on the high-resolution and wide-swath imaging, digital beamforming, and signal processing.

Zongsen Lv was born in Henan, China, in 1996. He received the B.S. degree in computer science and technology and the M.S. degree in software engineering from Henan University, Kaifeng, China, in 2018 and 2022, respectively. He is currently working toward the Ph.D. degree in communicaiton and information system with the Department of Space Microwave Remote Sensing System, Aerospace Information Research Institute, Chinese Academy of Sciences (CAS), Beijing, China.

He is currently with the University of CAS, Beijing. His scientific interest includes synthetic aperture radar (SAR) remote sensing, focusing on SAR signal processing, digital beamforming, and radio frequency interference mitigation.

Yuhao Wen was born in Hunan, China, in 1997. He received the B.S. degree in electronic information science and technology from Central South University, Changsha, China, in 2019. He is currently working toward the Ph.D. degree in communicaiton and information system with the Department of Space Microwave Remote Sensing System, Aerospace Information Research Institute, Chinese Academy of Sciences, Beijing, China.

He is also with the University of Chinese Academy of Sciences. His main research interests include multichannel synthetic aperture radar (SAR) signal processing, SAR waveform diversity, and SAR ambiguity suppression.

Zhen Chen (Member, IEEE) received the B.S. degree in communication engineering from Central South University, Changsha, China, in 2017, and the Ph.D. degree in communication and information system from the University of Chinese Academy of Sciences, Beijing, China, in 2022.

He was a Visiting Ph.D. Student with the Sapienza University of Rome, Rome, Italy, in 2022. He is currently a Special Research Associate (Postdoctoral Researcher) with the Aerospace Information Research Institute, Chinese Academy of Sciences, Beijing. His scientific interest includes synthetic aperture radar remote sensing, focusing on the high-resolution and wide-swath imaging, digital beamforming, signal processing, and motion compensation.

Zhimin Zhang received the B.S. degree in electrical engineering from the Beijing Institute of Technology, Beijing, China, in 1992, and the M.S. degree in communication and electronics system from the Graduate University of Chinese Academy of Sciences, Beijing, in 1995.

Since 1995, he has been with the Aerospace Information Research Institute, Chinese Academy of Sciences, where he has been working on radar system design and signal processing. His recent research interests include high-resolution wide-swath spaceborne SAR imaging, ship detection technology in SAR images, and SAR radio frequency interference mitigating technology.

Yifei Liu was born in Hebei, China, in 1999. He received the B.S. degree in electronic information engineering from Harbin Engineering University, Harbin, China, in 2020. He is currently working toward the Ph.D. degree in communication and information system with the Department of Space Microwave Remote Sensing System, Aerospace Information Research Institute, Chinese Academy of Sciences, Beijing, China.
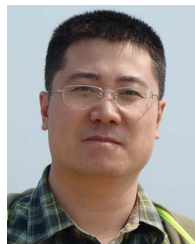
He is currently with the University of Chinese Academy of Sciences. His research interests include spaceborne inverse synthetic aperture radar imaging and signal processing.

Huaitao Fan received the B.S. degree in electronic information science and technology from the Ocean University of China, Qingdao, China, in 2012, and the Ph.D. degree in communication and electronics system from the University of Chinese Academy of Sciences, Beijing, China, in 2017.

He is currently with Aerospace Information Research Institute, Chinese Academy of Sciences, Beijing. His research interest includes azimuth multichannel synthetic aperture radar signal processing.

Lei Zhang received the B.S. degree in electrical engineering from the University of Science and Technology of China, Hefei, China, in 2008, and the Ph.D. degree in communication and electronics system from the University of Chinese Academy of Sciences, Beijing, China, in 2014.

He is currently an Associate Professor with Aerospace Information Research Institute, Chinese Academy of Sciences, Beijing. His research interests include high-resolution spaceborne/airborne synthetic aperture radar imaging and signal processing.